Journal of the Brazilian Society of Mechanical Sciences and Engineering (2024) 46:565
https://doi.org/10.1007/s40430-024-05137-w

TECHNICAL PAPER

Study of creep and creep crack growth fatigue of aging ASTM A297/A297M-19 HP steel modified with niobium

M. C. A. Gatti[1] · W. W. Bose Filho[1] · M. C. Carvalho[2] · C. O. F. T. Ruchert[1]

Received: 23 September 2023 / Accepted: 8 August 2024 / Published online: 22 August 2024

Abstract

The ASTM A297/A297M-19 HP steel is a commonly used material in high-temperature structural components. In this study, researchers examined the effects of niobium modification on the mechanical properties of HP steel. The tests included hardness, tensile, creep, fatigue, and metallographic analysis. The heat treatment of aging at 927 ºC for 1000 h resulted in the precipitation of secondary carbides and G-phase presence. The aging caused intense precipitation in the interdendritic space, where the chromium carbides coalesced and became coarser. The aged specimens showed an increase in hardness by approximately 17%. The tensile tests showed an increase in mechanical resistance parameters and a decrease in total elongation. The Charpy impact tests presented lower values at 927 ºC. In the creep tests, the stress exponent showed a sharp decrease at the highest temperature of 1093 ºC. The fatigue crack propagation rate was higher at 927 ºC than at 25 ºC due to the material's better ductility at high temperatures. In creep crack growth tests, a decrease in the crack growth rate was observed in the second stage. These experimental results are important for understanding the ability of the modified HP steel to withstand fatigue and creep mechanisms at elevated temperatures from a time-dependent fracture mechanics perspective.

Keywords High-temperature fatigue · Creep crack growth · Aging · Niobium

1 Introduction

Stainless steels are alloys primarily made of iron and chromium, with at least 10.5% chromium content [1]. When exposed to oxygen, they form a protective layer of chromium oxide, making them resistant to corrosion. Other elements like nickel, molybdenum, titanium, and niobium can be added to enhance their heat resistance.

HK and HP series stainless steels are commonly used in industries like petrochemicals for applications requiring high temperatures above 900 °C [2]. Over time, HP-40 grade stainless steel has been improved by adding elements like niobium, titanium, and yttrium to enhance its strength against creep deformation at high temperatures [3].

HP steel is widely used in structural components operating at temperatures up to about 1150 °C, with a typical working temperature of 927 °C [4]. The ASTM A297 standard [5] specifies these steels. The microstructure of HP steel consists of an austenitic matrix surrounded by primary carbides. The addition of niobium leads to secondary precipitation, resulting in a more stable microstructure at high temperatures [6].

Various studies have been conducted to understand the microstructural evolution and its effects on mechanical properties at high temperatures [7–9]. The addition of carbide-forming elements like niobium and yttrium has improved the intrinsic properties of high-temperature resistant stainless steels [2].

Hot deformation tests on materials like Incalloy 901 and HP-Nb steel have shown good workability at high temperatures [10]. Increasing temperature above 800 °C in HP-Nb steel reduces flow stress, indicating improved ductility due to dynamic recrystallization [11].

A study investigated the behavior of a specific type of steel, ASTM A297 HP steel, which had been modified with niobium, at high temperatures. The examination of fractured specimens revealed a tendency for the material to fracture

Technical Editor: João Marciano Laredo dos Reis.

✉ C. O. F. T. Ruchert
cassiusterra@usp.br

[1] Department of Materials, Engineering School of São Carlos, University of São Paulo, São Paulo, Brazil

[2] Federal University of the South and Southeast of Pará, -UNIFESSPA, Marabá, Brazil

along grain boundaries, indicating potential weaknesses in its structure [12].

Understanding the mechanical properties of materials under high temperatures is crucial for various applications [13].

Creep, the gradual deformation of materials under stress and heat, involves multiple factors such as stress, strain, temperature, and microstructure. This deformation process can result in various forms of damage, including voids, cracks, and structural alterations, eventually leading to material failure [14].

Researchers employed a deformation-mechanism-based true-stress (DMTS) creep model to study the behavior of modified 9Cr-1Mo steel under creep conditions. They observed distinct stress-dependent deformation mechanisms in different stress regions [15]. Furthermore, modifications were made to the DMTS model to incorporate the influence of oxidation on the steel's long-term creep performance, providing insights into failure modes related to intragranular and intergranular deformation [16].

Another critical parameter for understanding crack formation under creep conditions is the C^* parameter, which is analogous to the J-contour integral [17]. The C^* parameter is obtained experimentally using an expression that requires knowledge of the load line displacement rate due to creep. A mathematical expression gives the relevant parameter of creep crack growth in Integral-$C^*(t)$ of a line or surface surrounding the front of a crack linking from one crack surface to another crack surface. Thus, the expression $C^*(t)$ for a two-dimensional crack in the x–z plane with the crack front parallel to the z-axis is given by a line integral, according to the ASTM E 1457–13 standard [18], and is shown in Eq. (1),

$$C^*(t) = \int_{\Gamma} \left(W^*(t)dy - T\frac{\partial \dot{u}}{\partial x}ds \right) \tag{1}$$

where

$W^*(t)$ is the energy rate per unit of volume or instantaneous stress power;

Γ is the path of the integral that contains the crack tip;

ds is the increment in the contour path;

T outward traction vector on ds;

$\dot{u}$ is the displacement rate vector at ds;

x, y, z are axes of rectangular systems;

$T\frac{\partial \dot{u}}{\partial x}ds$ is the rate of stress-power input, within the area delimited by Γ.

In most cases, parameter C^* is used under stationary conditions and can be obtained numerically from an integral that does not depend on the path and is analogous to integral J's value for rates independent of the material's behavior. However, parameter C^* will be interpreted as a rate of released energy, analogous to the definition of the energy of J, using the stress reference method [19] described by Eq. (2),

$$C^* = -\frac{1}{B}\frac{dU^*}{da} \tag{2}$$

a is the crack length, B is the thickness of the specimen, and U^* is the potential energy rate. Thus, this equation can be used in laboratory tests instead of using the definition of linear integral. Besides, the reference stress of the creep strain interpretation method can be used to derive C^*. The reference and experimental stress methods are placed face to face as a proposed method for deriving C^*. However, validated numerical methods for derivation can also be used.

There are different ways to estimate the C^* parameter, which can be analytical, numerical, experimental, or a combination of these. An experimental measurement of C^* can be obtained by testing specimens in the laboratory, where a high-precision experimental measurement of the parameter can be determined. For component characterization, the ASTM E1457-13 standard [18] will be followed, and the methods adopted for calculating C^* will be in accordance with Saxena [19].

The value of parameter C^* can be determined directly from the applied load line's displacement rate. The value of C* is calculated using Eq. (3).

$$C^* = \frac{P\dot{V}}{B_N(W-a)}F' \tag{3}$$

where P is the applied load, W is the width of the specimen, a is the crack length, B_N is the net thickness after lateral notch, F' is a function of the material properties in creep (n) and a geometric factor, and $\dot{V}$ is the value of the displacement rate measured on the load line at the stationary stage. The value of n is determined through the creep tests' results, this being the stress exponent of Norton's Law, as determined by Eq. (4) [19],

$$\dot{\varepsilon}_s = A\sigma^n \tag{4}$$

A is a constant characteristic of the material, n is the stress exponent, σ is the applied stress and $\dot{\varepsilon}_s$ steady-state creep rate in the secondary stage.

Equation (2) can be rewritten with all the data related to displacement on the load line, called "*FLD*" [20]; therefore, the value of C^* can be calculated by Eq. (5),

$$C^* = \frac{P\dot{V}^{FLD}}{B_N(W-a)}H^{FLD}\eta^{FLD} \tag{5}$$

$\dot{V}^{FLD}$ is the displacement rate in the load line at the stationary stage; H^{FLD} and η^{FLD} are geometric functions according to the type of specimen adopted in the project.

For the type of specimen C(T), which will be adopted in this article, geometry and dimensions are according to the ASTM E1457-13 standard [18], the geometric function H^{FLD} is given by Eq. (6);

$$H^{FLD} = \frac{n}{n+1} \tag{6}$$

and the value of the function η^{FLD} is a dimensionless value established by Table A 2.1 in the ASTM E1457-13 standard [18].

In Eq. (6), n is the stress exponent of Norton's Law obtained in the creep test, according to the ASTM E139-10 standard [21].

The value of parameter C^* can be obtained experimentally using Eq. (7) [15],

$$C^* = \frac{P\dot{V}_s}{B_N W}\eta\left(\frac{a}{W}, n\right) \tag{7}$$

in Eq. (7), P is the applied load, W is the width of the specimen; a is the crack length, B_N is the net thickness after lateral notch, $\dot{V}_s$ is the value of the displacement rate measured on the load line at the stationary stage, n is the stress exponent of Norton's Law from Eq. 4 and η is a time-dependent geometric function. For type C(T) specimen, the value of η [18] is calculated using Eq. (8),

$$\eta = \frac{n}{n+1}\left[\frac{2 + 0,522\left(1 - \frac{a}{W}\right)}{\left(1 - \frac{a}{W}\right)}\right] \tag{8}$$

The potential drop method is a technique that involves monitoring the growth of a crack by measuring the potential difference generated between the two sides of the crack mouth using direct current on the C(T) specimen. As the crack propagates, the specimen's electrical resistance tends to increase, which helps to correlate the potential drop with the size of the crack. The crack length was determined using Eq. (9) from Annex A3 of ASTM Standard E 1457–13 [18].,

$$a = \left[(a_f - a_0)\left(\frac{V - V_0}{V_f - V_0}\right)\right] + a_0 \tag{9}$$

in Eq. (9), a_0 and a_f are the average starting and ending crack length, V_0 and V_f are the starting and ending voltage measured directly on the specimen, and V is the instantaneous voltage for a given crack length a.

The values of a_0 and a_f are measured on the specimen's fracture surface after the test.

New techniques have been developed to improve the creep contribution to the load line displacement rates during creep crack growth tests [22].

Although several studies have been carried out on creep crack growth in several types of stainless steels such as 316N [23], 316H [24], 304 [25], 304L [26], 308 [27], and 709 [28], few studies are found in the literature on ASTM A297 steel modified with niobium.

In this work, the Nb modified ASTM A297/A297M-19 HP stainless steel's high-temperature mechanical behavior was investigated in the microstructural conditions as cast and aging at 927 ºC for 1000 h, through mechanical tests of hardness, tensile, creep, fatigue, and metallographic analyzes. The fracture parameter C^* of the time-dependent fracture mechanics was calculated. Creep testing and creep crack growth were performed at various stress levels to determine the material constants necessary to calculate the C^* fracture parameter. It was possible to model a relationship between the crack propagation rate by the creep of *da/dt* as a function of the fracture parameters.

2 Experimental procedure

The material under investigation, cast steel ASTM A297/A297M-19 HP, was modified with niobium and analyzed in its raw state. This steel, cast by gravity in a sand mold, is of significant interest due to its unique properties. The "*Y*" shape casting part, as seen in Fig. 1, was used for the experiment.

The decreased volumetric fraction of secondary precipitation with increased niobium content may explain the relatively lower rupture time. The literature indicated the optimal composition of niobium 1.2% is the best fit for

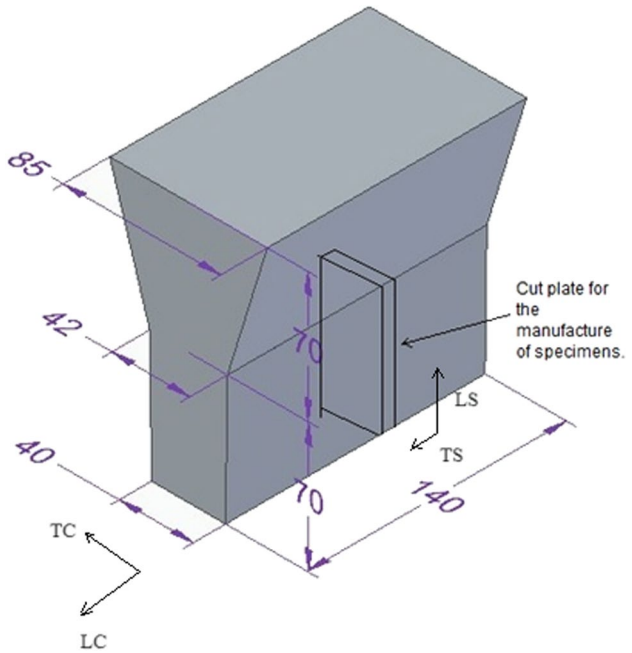

Fig. 1 Geometry and dimensions are given in millimeters of casting part made of steel ASTM A297/A297M-19 HP Grade HP niobium modified steel and the location of specimens (TC = Transverse Cast direction, LC = Longitudinal Cast direction, TS = Transverse Sample direction, and LS = Longitudinal Sample direction)

mechanical properties [29]. Experimental data proved that after aging at 700 ºC and 900 ºC for 1000 h. The material was placed in an electric resistance furnace built by the foundry and then cooled in calm air. The furnace controller was calibrated using Ecil type K thermocouples on a Fluke 714B temperature calibrator. The niobium carbides became unstable and tended to turn into a silicide, described as the G-phase. However, close to 1100 ºC, this phenomenon did not occur [30]. The part shown in Fig. 1 was obtained by static sand casting, which is a technology that has existed for millennia in the process of manufacturing metallic castings; this process involves filling a mold's cavity with liquid metal using gravity. As the metal solidifies, it takes on the mold's shape and dimensions, corresponding to the part to be manufactured.

The upper part of the casting was removed, and the lower central part of the piece was cut in the transverse direction. The plate was divided in half through a cut in the longitudinal direction. One of the halves remained in the condition as-cast, and the other half underwent an aging treatment at 927 ºC for 1000 h. The material as-cast was named AC, and the heat-treated material was named T1000. The specimens were machined in the plate's longitudinal direction, as shown in Fig. 1.

Chemical analysis was performed employing spark emission spectroscopy (ARL 3460) of the material in the as-cast condition. The analysis temperature was 25 ºC. The microstructural analysis was performed on the material samples in the AC and T1000 conditions before and after the mechanical tests.

The samples were mounted in conductive Bakelite, ground with sandpaper of granulometry # 80, 120, 220, 400, 600, 800, 1200, and 2000 and polished with diamond. After polishing, a chemical attack was performed on each sample's surface to allow the observation of the micro constituents. For the material under study, the reagent used was "regal water," which consists of a solution of 3 parts of hydrochloric acid and 1 part of nitric acid. The average duration of exposure of the material to the chemical reagent was approximately 30 s. Microstructural observations and acquisitions were carried out using an optical microscope Carl Zeiss Microlmaging GmbH, coupled to the AxioCam ERc5s camera.

The fracture surfaces of the material in the different conditions and from the different tests were analyzed by scanning electron microscopy (SEM) in a FEG Model InspectTM F50MEV to verify the fracture morphologies in the crack propagation and final fracture regions.

The Vickers hardness tests were performed on the tensile test specimens samples following the ASTM E-92–03 standard [31]. The indenter used was a diamond pyramid with a load of 10 Kgf. The previously prepared samples were ground with # 80, 120, 220, 320, 400, 600, 800, and 1200 sandpaper and then polished with chromium dioxide. Six hardness measurements were made on three samples for both AC and T1000 conditions. The equipment used was a digital Leco hardness tester.

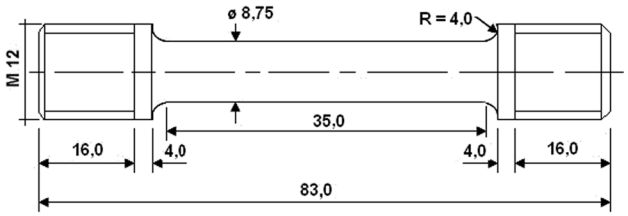

Fig. 2 Geometry and dimensions are given in millimeters of the specimen used in the tensile test

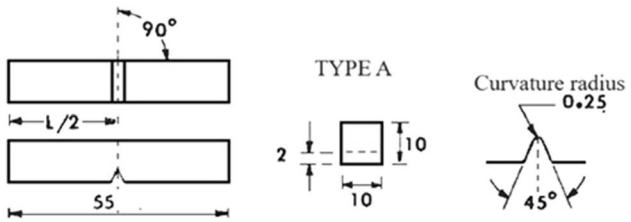

Fig. 3 Geometry and dimensions are given in millimeters of the specimen used in the impact test

The tensile tests were performed on specimens machined from the material in the AC and T1000 conditions, according to the ASTM E-8M-11 [32] (25 ºC) and ASTM E-21-09 [33] (high temperatures) standards. These were carried out on a universal servo-hydraulic testing machine MTS 810 with 250 kN capacity, equipped with accessories for testing at low and high temperatures. For the execution of the tests at high temperatures, the specimens were heated through an induction furnace Inductoheat, type LSS 7.5 kW/200 kHz, and temperature measurements were made using an optical pyrometer Raytec (D9ETXSLTCF1L2). The geometry and dimensions of the tensile specimen are shown in Fig. 2.

The impact tests were performed on Charpy specimens with V-notch, shown in Fig. 3, in the AC and T1000 condition, at temperatures of 25 ºC and 927 ºC. The tests were carried out on specimens with conventional and pre-cracked notches, according to the ASTM E-23-12 standard [34], seeking to initially verify the sensitivity of the material to the type of notch. The preparation of a 1.0 mm pre-crack, from the root of the notch, in each specimen, was performed on a servo-hydraulic machine MTS model 810, under a frequency of 30 Hz, load ratio R = 0.1, maximum load of 4.5 kN and room temperature. Three specimens were used for each condition.

The creep tests were performed with constant stresses of 36, 40, 50, and 60 MPa at a temperature of 927 °C, using a high-temperature extensometer for deformation

measurement as a function of time to the ASTM E-139-11(2018) standard [21]. The creep curve can be obtained at different stress levels, which helps calculate the creep rate values during the secondary or stationary stage. As outlined in Eq. (7), this information can then be used to derive parameters A and n in Norton's correlation. The creep curves obtained made it possible to determine the level of resistance to 1.0% strain in the conditions AC and T1000. Different test temperatures, ranging from 800 to 950 ºC in the AC condition, were adopted.

The geometry and dimensions of the specimen used in conventional creep tests are shown in Fig. 4.

The fatigue tests, using the ε-N methodology, were performed under strain control, according to the ASTM E-606-12 standard [35]. Specimens in the T1000 condition were tested at temperatures of 25 ºC and 927 ºC. Six levels of total deformation amplitude were used for the temperature of 25 ºC, and five levels at 927 ºC to determine the ε-N curve. The tests were performed on a 250 kN capacity MTS servo-hydraulic Machine, using a sine wave, frequency of 2 Hz, and reverse strain ratio, $R = -1.0$. Strain control was performed using MTS strain gauges suitable for testing at high temperatures. The geometry and dimensions of the fatigue specimens are shown in Fig. 5.

An induction furnace heated the fatigue specimens, and temperature measurements and control were made using an infrared optical pyrometer equipped with a laser sight. This sensor's temperature served as a control parameter for the induction furnace.

The mechanical behavior of the steel was evaluated through cyclic stress–strain hysteresis and by strain-life curves: total strain amplitude ($\Delta\varepsilon_t/2$), plastic strain amplitude ($\Delta\varepsilon_{Pl}/2$) and elastic strain amplitude ($\Delta\varepsilon_{el}/2$), as a function of the number of reverses to fail (2Nf), according to the Coffin-Manson relationship [36].

The fatigue crack propagation tests were performed on type C(T) specimens, as shown in Fig. 6, according to the ASTM E-647–13 standard [37], in the AC and T1000 conditions at temperatures of 25 ºC and 927 ºC. Both pre-cracks and fatigue crack propagation tests were performed under a frequency of 5 Hz and load ratio R = 0.1, and the crack growth was measured with the same strain gauge used to measure the strain in the ε-N test, which was coupled in the V_0 position of the C(T) specimen, according to the ASTM E-647-13 standard.

The heating of the C(T) specimens for the tests performed at 927 ºC was carried out in a muffle furnace, coupled to a digital temperature controller. Inconel grips were used to perform the high-temperature testing; a grip cooling system was also used.

The creep crack growth tests were carried out at a temperature of 927 ºC, in the AC condition, in a Constant Load Creep Test System designed and developed by the Mechanics and Fracture Group of the Materials Engineering Department to operate according to ASTM E1457-13 standard

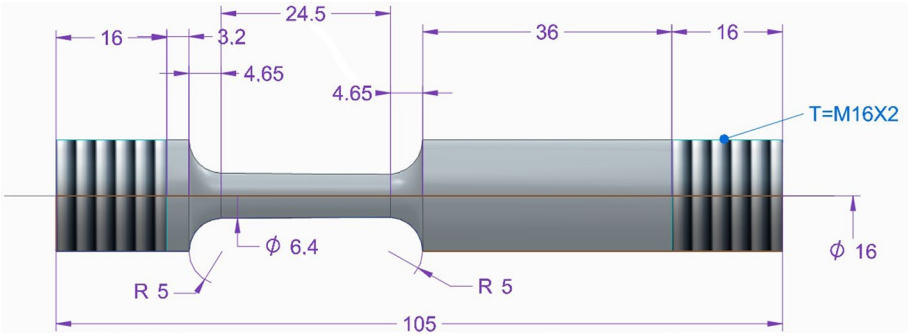

Fig. 4 Geometry and dimensions are given in millimeters of the specimen used in the conventional creep test

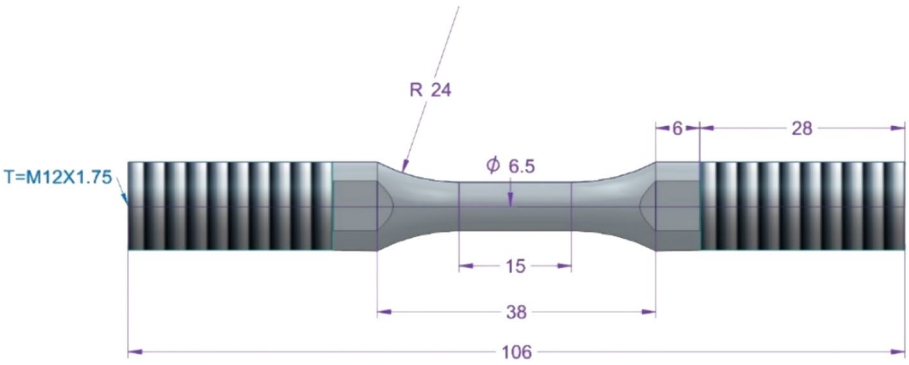

Fig. 5 Geometry and dimensions are given in millimeters of the specimen used in the fatigue test

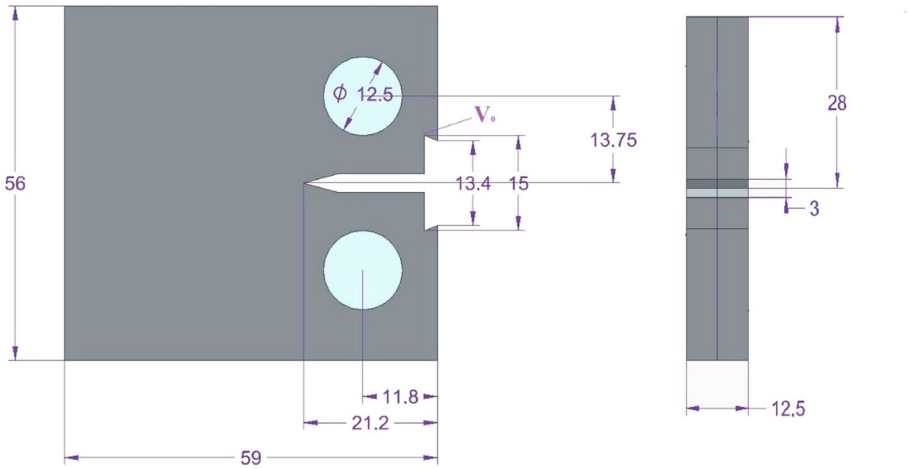

Fig. 6 Geometry and dimensions are given in millimeters of the specimen used in the fatigue crack propagation test

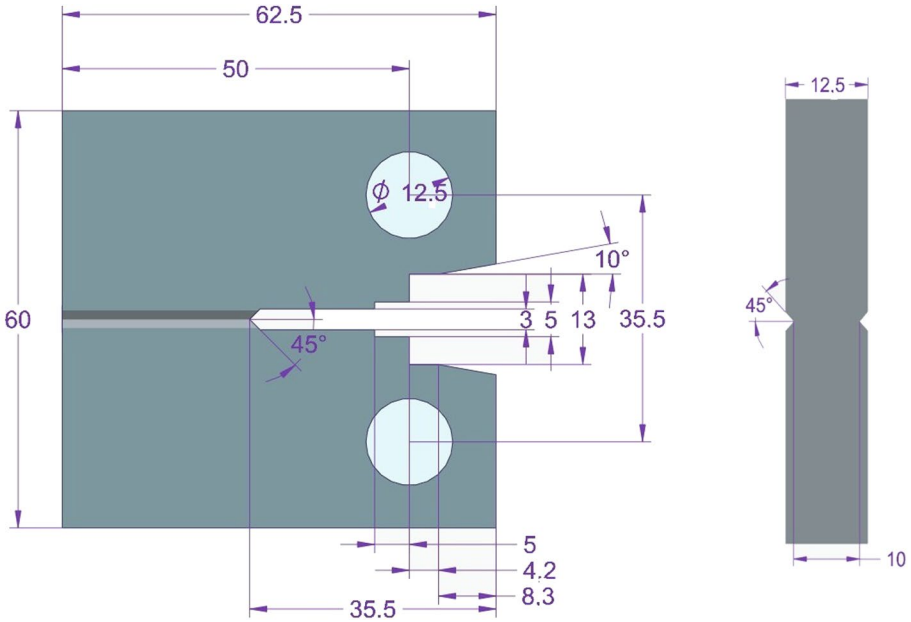

Fig. 7 Geometry and dimensions of type C(T) specimen used in creep growth tests in millimeters

[18]. The fatigue crack growth test was performed according to the ASTM E2760-10 standard [38] in a 100 kN MTS LandMark Servo-Hydraulic Test System. The specimens used in the two tests were of type C(T), with the geometry and dimensions, as shown in Fig. 7. Two different values K_i of initial stress intensity factor were used in the tests: $K_i = 6.8$ MPa $m^{1/2}$ and $K_i = 5.5$ MPa $m^{1/2}$.

The creep crack growth measurements were performed using the electrical potential difference method described in Annex A4 of the ASTM E1457-13 standard [18] and shown in Fig. 8. An extensometer with a high-temperature ceramic rod positioned on the specimen's load line was used to measure its displacement from the load line.

The values of crack size and load line displacement measured as a function of time were necessary to obtain the material's *da/dt—C** curve.

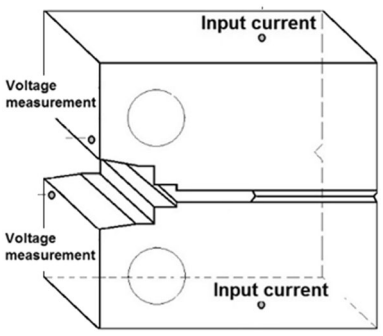

Fig. 8 Schematic drawing indicating the locations of the current input and voltage output points for data acquisition in the creep crack growth test

Using the data obtained in creep crack propagation tests, the crack growth rate (*da/dN*) as a function of *C** of the ASTM A297/A297M-19 Grade HP niobium modified steel in the as-cast (AC) condition can be determined.

The peripherals and equipment used in determining the rate of crack propagation rate by creep as a function of parameter *C** are shown in Fig. 9.

3 Results and discussion

The chemical composition, performed on a sample of the AC condition, was analyzed by optical emission spectroscopy (OES), and the results are shown in Table 1. In this way, it can be observed that the chemical elements are within the nominal range specified by the ASTM A297/A297M-19 standard [5].

An austenitic matrix surrounded by primary carbides (Cr_7C_3), NiC, and NbC is observed in the AC sample, see Fig. 10a, mainly in the interdendritic orientation. In the T1000 sample, see Fig. 10b, the precipitation of secondary carbides ($Cr_{23}C_6$) is noted within the austenitic matrix, and the presence of phase G, composed of niobium and nickel carbides [9]. Thus, the heat treatment provided intense precipitation in the interdendritic space, where the chromium carbides coalesced and became coarser, whereas the niobium carbides did not undergo significant changes.

Table 2 presents the average result obtained in the Vickers hardness tests. The results showed an increase in hardness with the samples' aging process. This increase is most likely attributed to the increasing presence of the component hard phase in the microstructure [39].

The results obtained in the tensile tests up to fracture for the conditions AC and T1000 as a function of the test temperature for a test speed of 2.0 mm/min are shown in Fig. 11. It can be seen that the curves obtained in the test show practically the same behavior in the AC condition, see Fig. 11b. In the T1000 condition, see Fig. 11b, serrations are observed in the tensile curves related to high temperatures, characterizing the discontinuous plastic flow, that is,

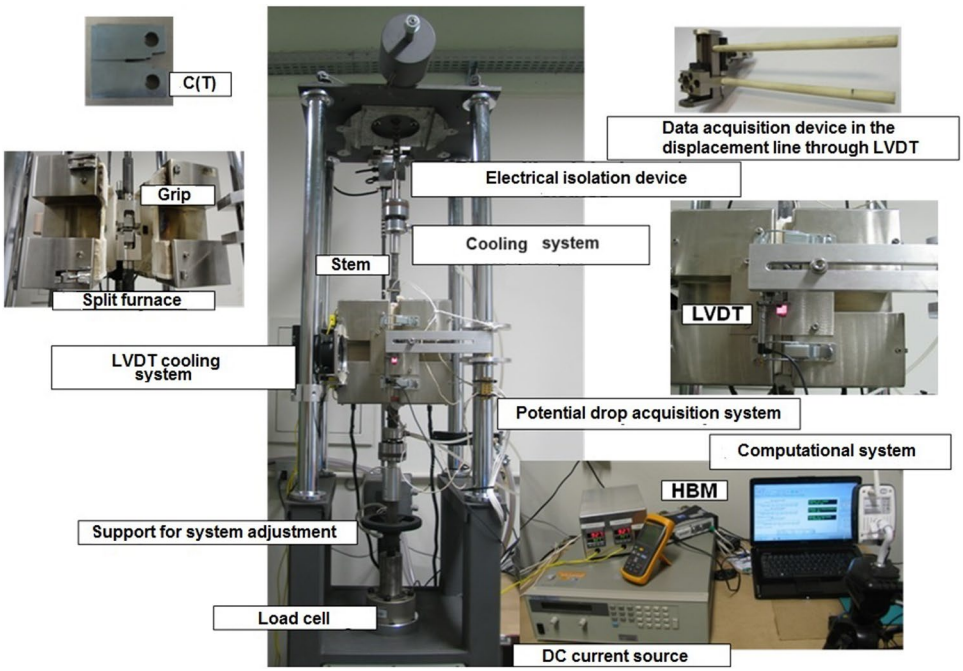

Fig. 9 Equipment and peripherals used in creep crack growth tests

Table 1 Chemical compositions (wt. %) of the sample AC ASTM A297/A297M-19 HP niobium modified steel and standard chemical composition (SC), measured by OES

Sam	C	Si	Mn	P	S	Cr	Ni
AC	0.40	1.10	1.11	0.018	0.004	25.70	35.8
SC	0.35–0.75	0.75(max.)	2.00(max.)	0.04(max.)	0.04(max.)	24–28	36–37

Mo	Cu	Nb	Fe
0.085	0.088	1.01	Bal
0.5(max.)	0.25(max.)	1.0–1.5	Bal

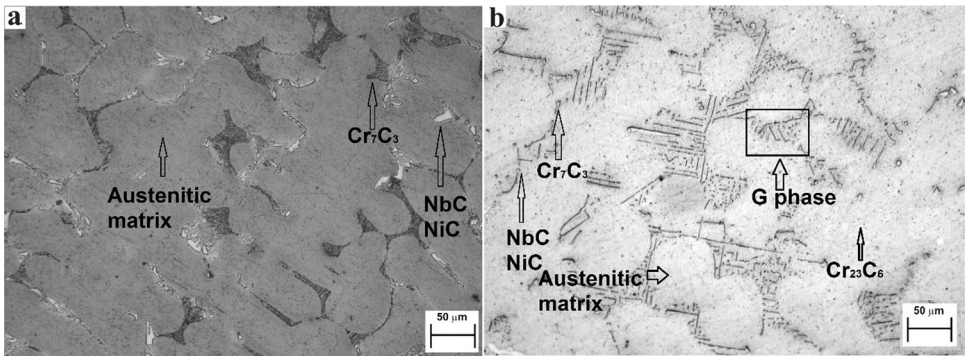

Fig. 10 Optical images of etched cross-sectional surfaces of the ASTM A297 HP niobium modified steel. **a** Presenting an austenitic matrix surrounded by primary carbides (Cr_7C_3), NiC, and NbC is observed (AC). **b** Showing the precipitation of secondary carbides ($Cr_{23}C_6$) within the austenitic matrix and the presence of phase G (T1000)

Table 2 Results of Vickers hardness testing

As-Cast	T1000
170.5 ± 10.0 HV	193.8 ± 5.6 HV

the Portevin–Le Chatelier effect (PLC). The tensile curve's PLC effect is a classic aspect of dynamic aging observed in low and medium carbon steels, indicating that dynamic aging (DSA) has similar characteristics [40].

The impact test results obtained at room temperature were lower than those from 927 °C in all conditions tested, as shown in Fig. 12a, and Table 3. Therefore, the strengthening of the austenitic matrix increased energy absorbed by impact with thermal aging. When it comes to comparing the results obtained in conventional notched and notched specimens with pre-crack, it is noted that, for both conditions, AC and T1000, the material exhibited notch sensitivity. The pre-cracked specimens obtained 10–28% smaller energy than the specimens without pre-cracking for the same test temperature. The tunneling shown in Fig. 12b was found in the fatigue pre-crack propagation in an impact specimen's fracture region after being tested. The material fails due to microvoid coalescence, and tunneling starts in the interior and spreads towards the surface [41].

Comparing the same conditions AC and T1000, see Fig. 13, at a temperature of 927 ºC, it presented a ductile fracture, accompanied by oxidation of the fracture surface. A mix of ductile fracture with a fragile interdendritic fracture is noted at 25 ºC, with a more significant predominance of the former. These evaluations corroborate the results obtained in the tensile and impact tests.

The results obtained of the specimens tested at a temperature of 927 ºC in the conditions AC and T1000 shown in Table 3 demonstrated that aging's heat treatment increases the material's creep life. This better resistance can be attributed to the precipitation of secondary carbides in the matrix. Creep tests have shown the importance of secondary precipitation and indicated the more significant contribution of Phase G to the creep strength [29].

The Norton relation is reasonably well defined by straight lines, in the log–log diagram, at each temperature level, see Fig. 14. In the range of 871–1066 ºC, the n varies between approximately 8.3 and 9.8. For 1093 ºC, the value of *n* from the stationary creep rate drops to 5.8, as shown in Table 4. The decrease in stress exponent at high temperatures is

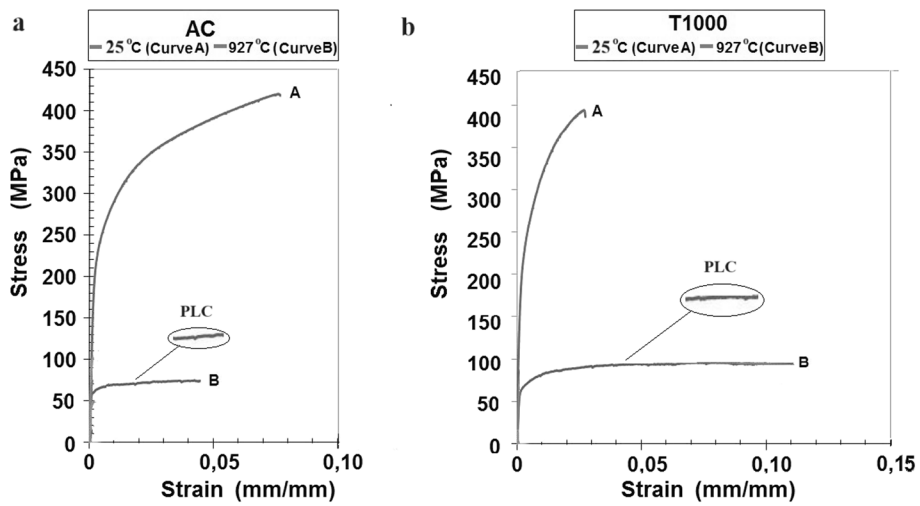

Fig. 11 Tensile engineering curves up to fracture of the ASTM A297/A297M-19 HP niobium modified steel in condition: **a** AC and **b** T1000

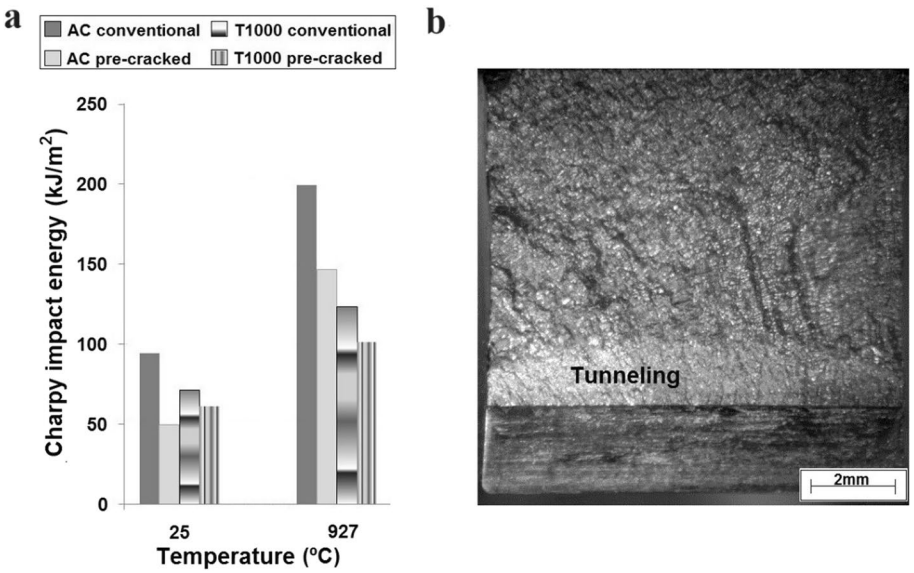

Fig. 12 **a** Results of Charpy impact energy at 25 °C and 927 °C of the ASTM A297/A297M-19 HP niobium-modified steel. for AC and T100 conditions. **b** Stereographic image from the fracture surface of a specimen pre-cracked by fatigue and fractured in a Charpy impact test showing crack tunneling

Table 3 Creep test results for the ASTM A297/A297M-19 HP niobium modified steel of the AC and T1000 samples

Material	T (ºC)	σ (MPa)	$\dot{\epsilon}_{min}$(%/ h)	t_r (h)	A_r (%)	RA (%)
AC	927	60	2.1731	6.30	32.9	58.4
T1000	927	60	1.1881	12.05	40.2	52.0

where T = temperature, σ = stress, $\dot{\epsilon}_{min}$ = minimum creep rate, t_r = rupture time, A_r = rupture elongation, and RA = reduction of area

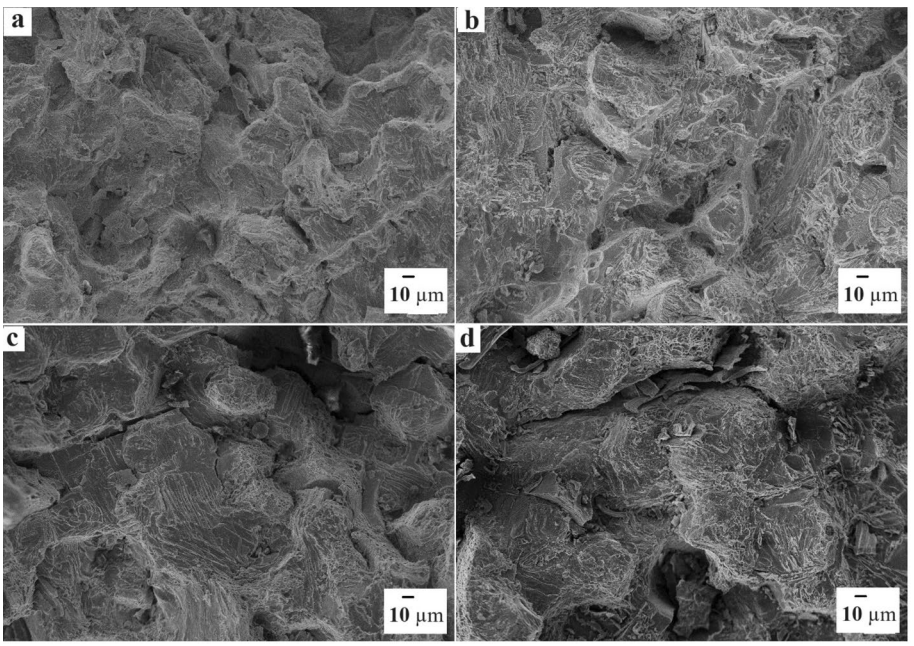

Fig. 13 SEM images of the fracture region of conventional specimen's impact tested on temperatures: **a** AC at 25 ºC, **b** AC at 927 ºC, **c** T1000 at 25 ºC, and **d** T1000 at 927 ºC

actually due to the transition into a dislocation-climb-controlled mechanism zone [15]. Towards a lower temperature of 871 ºC, it is probably grain boundary sliding (GBS).

The hysteresis obtained from cycles close to the failure of specimens tested in fatigue by controlling the strain amplitude is shown in Fig. 15. Note that the portion of the amplitude of plastic deformation is more significant at the temperature of 927 ºC, shown in Fig. 14b, than at the temperature of 25 °C, shown in Fig. 15a. Probably due to a result of deformation mechanism changing from rate-independent

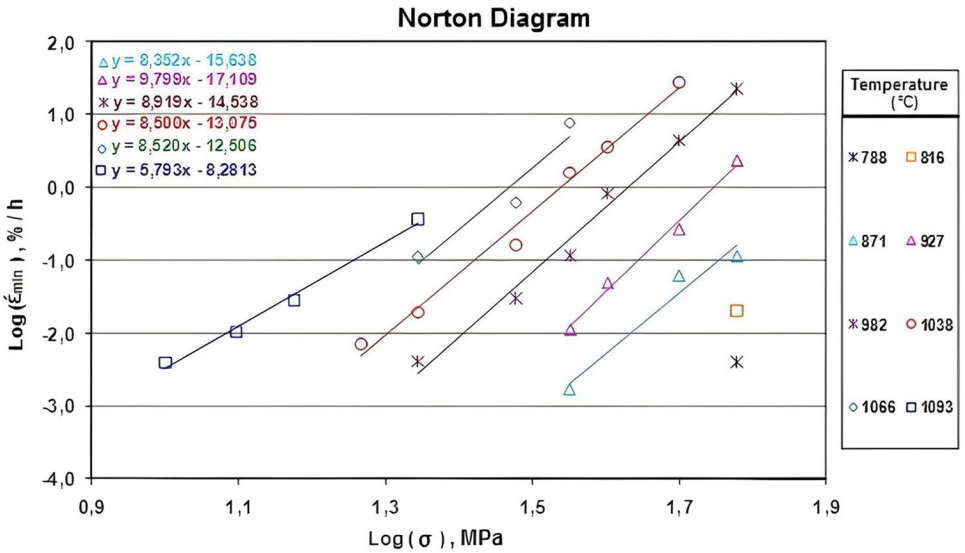

Fig. 14 Variation of the minimum creep rate with the stress of the ASTM A297/A297M-19 HP niobium modified steel, showing the value of the stress exponent *n* at each temperature level

Table 4 Results of the stress exponent of creep tests in the AC condition of the ASTM A297/A297M-19 HP niobium-modified steel

Temperature (ºC)	*n*	*A* ($MPa^{-n}h^{-1}$)	σ(MPa)	$\dot{\epsilon}_{min}(\%h^{-1})$
871	8.352	1.615 E-16	60	0.1137
927	9.799	4.442 E-19	60	2.3197
982	8.919	3.132 E-15	60	22.6567
1038	8.500	1.924 E-14	50	27.3754
1066	8.520	5.112 E-13	35.5	7.6833
1093	5.793	5.994 E- 9	22.1	0.3682

where: T = temperature, n = stress exponent, A = material constant, σ = stress, and $\dot{\epsilon}_{min}$ = minimum creep rate

plasticity via dislocation glide, to rate dependent plasticity, grain boundary sliding, as well as oxidation [42].

The fatigue life transition value, $2N_t$, of the T1000 material tested at 25 ºC (1900 reversals) shown in Fig. 16a, is less than that tested at 927 ºC (5000 reversals), see Fig. 16b. It is known that this parameter represents the life corresponding to the intersection between the elastic and plastic curves, that is, the life in which the stable hysteresis cycle has the same amount of elastic strain as the plastic. One factor corroborates with the increase of $2N_t$, at a temperature of 927 ºC, because the T1000 condition has increased ductility and changes in the deformation mechanisms at high temperatures.

It is noted that, for the same amplitude of total strain, the fatigue life of the material tested at 25 ºC is much greater than the fatigue life at 927 ºC as shown in Fig. 17, mainly in the high cycle fatigue region, above 104 cycles, where there is the domain of rate-independent plasticity via dislocation glide mechanism in the material. The fact that at 927 ºC, the fatigue life reduction can be attributed to two time-dependent factors: premature nucleation resulting from a significant

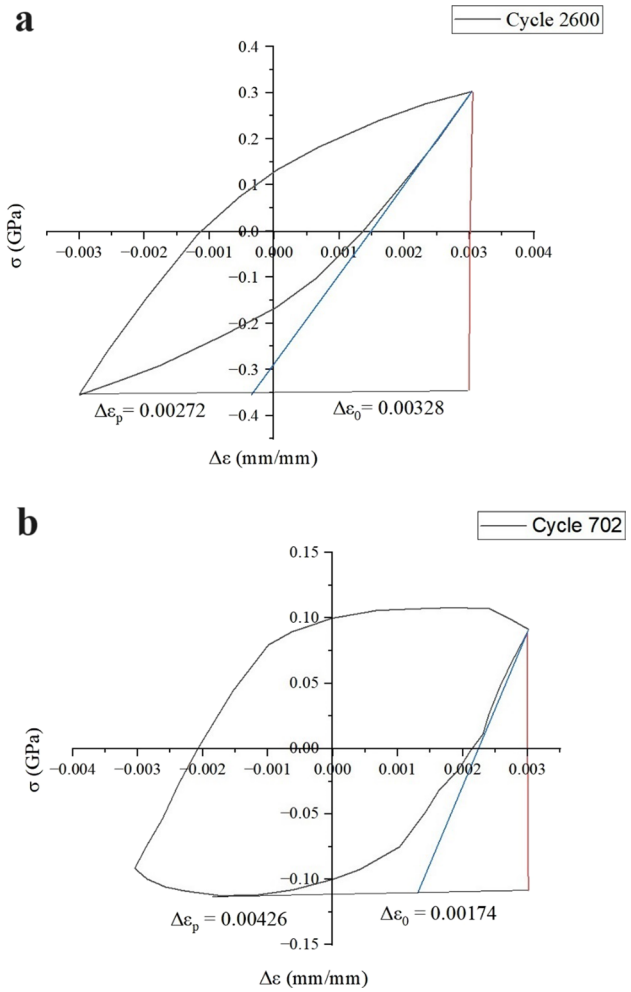

Fig. 15 Hysteresis obtained in ε-N fatigue tests with 0.30% total strain amplitude control of the ASTM A297/A297M-19 HP niobium modified steel: **a** 2500 cycle for the T1000 specimen tested at 25 ºC and **b** 702 cycle for the T1000 specimen tested at 927 ºC

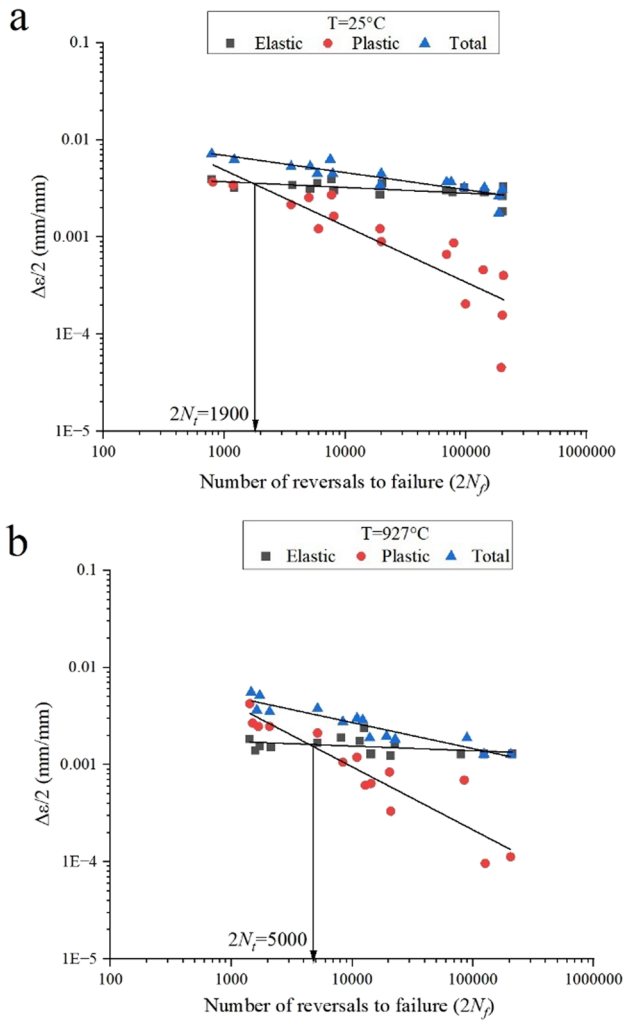

Fig. 16 Strain-life curves of the ASTM A297/A297M-19 HP niobium modified steel of the T1000 condition at temperatures of **a** 25 ºC and **b** 927 ºC

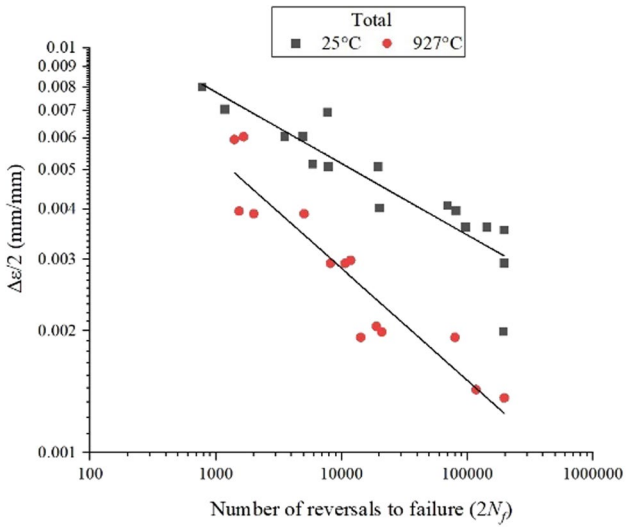

Fig. 17 The overlap between the total portions of the strain-life curve of the ASTM A297/A297M-19 HP niobium modified steel of the T1000 material at temperatures of 25 ºC and 927 ºC

reduction in the yield limit and the effect of the superficial oxidation of the slip bands premature crack nucleation.

A summary of the parameters obtained in the low-cycle fatigue tests is shown in Table 5. The total strain equations, $\Delta\varepsilon/2$, of material T1000, tested by fatigue at temperatures of 25 ºC and 927 ºC, are presented in the respective Eq. (10)–(11),

$$\Delta\varepsilon/2 = 0.0056\left(2N_f\right)^{-0.055} + 0.29\left(2N_f\right)^{-0.58} \quad (10)$$

$$\Delta\varepsilon/2 = 0.0026\left(2N_f\right)^{-0.054} + 0.55\left(2N_f\right)^{-0.69} \quad (11)$$

Figure 18 shows the curve of fatigue crack propagation rate, *da/dN*, as a function of the variation in the stress intensity factor, ΔK_I, in the Paris Region and the AC and T1000 conditions, obtained at temperatures of 25 ºC and 927 ºC. Thus, at the same ΔK_I level, the crack's propagation speed by fatigue is more significant in the material tested at 927 ºC than at 25 ºC for both microstructural conditions. This significant increase in the crack propagation rate, at 927 ºC, is due to a fatigue striation formation mechanism, which supposes that the growth of fatigue crack develops through a shear non-cohesive mechanism, by the slip bands at the crack tip [43]. This mechanism of striation formation by the plastic flow of the slip bands at the crack tip considers that an irreversible strain during each loading and unloading cycle results in the production of "ripples" with their size loading cycle increased on the fracture surface; they are striated due to more significant plasticity of the material tested at high temperatures [44].

The fatigue crack propagation tests carried out at 25 ºC and 927 ºC showed that both microstructural conditions exhibited a wide spread of the fatigue crack propagation rate in the Paris propagation region of the curve *da/dN* versus ΔK [36]. This behavior may be associated with short-range microstructural heterogeneity, which occurs in cast materials. Table 6 presents the Paris Equation parameters obtained in the fatigue crack propagation tests (Fig. 19).

From the parameters presented in Table 6, the Paris equations, in the AC and T1000 conditions, tested at temperatures of 25 ºC and 927 ºC, can be calculated using Eq. (12)–(15):

$$da/dN = 8.3 \times 10^{-11}(\Delta K)^{4.53}\ AC\ 25°C \quad (12)$$

$$da/dN = 1.6 \times 10^{-11}(\Delta K)^{4.10}\ AC\ 927°C \quad (13)$$

$$da/dN = 5.1 \times 10^{-14}(\Delta K)^{6.91}\ T1000\ 25°C \quad (14)$$

Table 5 The ASTM A297/A297M-19 HP niobium modified steel T1000 material low cycle fatigue parameters

Temperature	E (GPa)	Elastic strain			Plastic strain	
		$\sigma'_f(MPa)$	σ'_f/E	b	σ'_f	c
25 ºC	175	980	0.0056	−0.055	0.29	−0.58
927 ºC	70.8	184	0.0026	−0.054	0.55	−0.69

where: E = Young's modulus, σ'_f = fatigue strength coefficient, b = fatigue strength exponent, ϵ'_f = fatigue ductility coefficient, and c = fatigue ductility coefficient

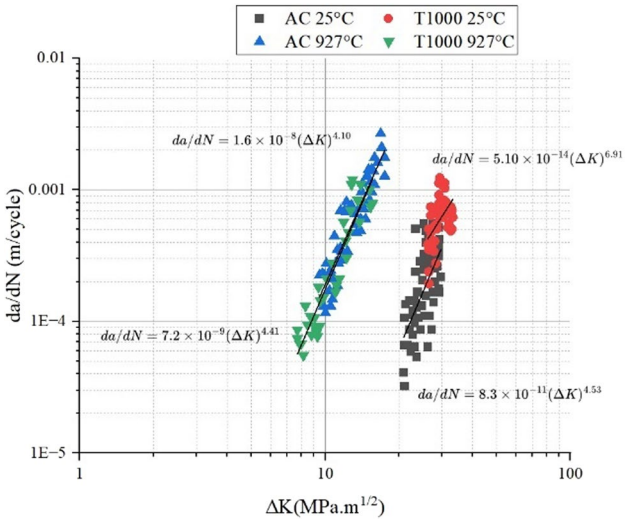

Fig. 18 The *da/dN* versus ΔK curve in the Paris region of ASTM A297 / A297M-19 HP niobium modified steel specimens for AC and T1000 conditions tested at 25 ºC and 927 ºC

Table 6 Parameters of the Paris equation for ASTM A297/A297M-19 HP niobium modified steel specimens for AC and T1000 conditions tested at temperatures of 25 ºC and 927 ºC

Conditions	Temperature	Paris equation parameters	
		C	m
AC	25 ºC	8.3×10^{-11}	4.53
AC	927 ºC	1.6×10^{-8}	4.10
T1000	25 ºC	5.1×10^{-14}	6.91
T1000	927 ºC	7.2×10^{-9}	4.41

where: C = Paris equation coefficient and m = Paris equation exponent

$$da/dN = 7.2\times10^{-9}(\Delta K)^{4.41}\ T1000\ 927\ ^{\circ}C \quad (15)$$

The result obtained for the increase in crack length as a function of time for the condition AC in two initial stress intensity factors: $K_I = 6.8$ MPa m$^{1/2}$ and $K_I = 5.5$ MPa m$^{1/2}$ is shown in Fig. 20a. The values of the length of the initial cracks measured in the specimens after total fracture was 26.1 mm for the specimen subjected to the stress intensity factor of $K_I = 6.8$ MPa m$^{1/2}$ and 27.2 mm for $K_I = 5.5$ MPa m$^{1/2}$. The specimen subjected to the initial stress intensity factor (K_I) of lesser value showed a decrease in the smaller crack's growth rate in the stable propagation stage compared to the specimen that was requested by an initial stress intensity factor greater K_I. In superalloys that have received standard heat treatments, a discrete distribution of grain boundary precipitates (e.g., $M_{23}C_6$ or G-phase) is often present, and its effect is to increase creep-rupture resistance by suppressing GBS [42].

The curves showing the increase in the displacement of the load line as a function of time for the two loads is shown in Fig. 19b, as it was through these two curves that it was possible to determine the relationship between the crack growth rate of *da/dt* versus the parameter C^* of time-dependent stress intensity.

The creep crack-growth rate da/dt as a parameter C^* function is shown in Fig. 19c. The relationship da/dt versus C^* can be represented by Eq. (16):

$$da/dN = 1.1\times10^{-3}(C^*)^{0.78} \quad (16)$$

Figure 19c also shows the results of creep crack growth rates as a function of parameter C*, obtained for a *Ni* superalloy called IN100 [45]. From the analysis of the results of this work, it can be concluded that the alloy ASTM A297/A297M-19 HP niobium modified, in the as-cast condition, presents creep crack growth rates of approximately ten times higher for low C^* values when compared to the superalloy IN100 in the as-cast condition.

Figures 20 and 21 also show the macro and micro fractographic aspects, obtained by the SEM technique, of the fracture surfaces of the two specimens fractured in the creep crack growth tests in the AC condition tested at 927 ºC.

In Fig. 20 and Fig. 21, point 1 refers to the pre-fatigue crack region where the planar morphological aspect typical of fatigue crack propagation can be noted. At point 2, a fracture morphology is observed, a typical aspect of slow propagation by creep, where an interdentritic morphology is observed, as well as the severe oxidation process, due to the long period of residence at a temperature of 927 ºC, which may also have contributed to an intergranular propagation process (interdendritic), in this case, the fracture surface presents a typically brittle behavior, as expected for an as-cast condition.

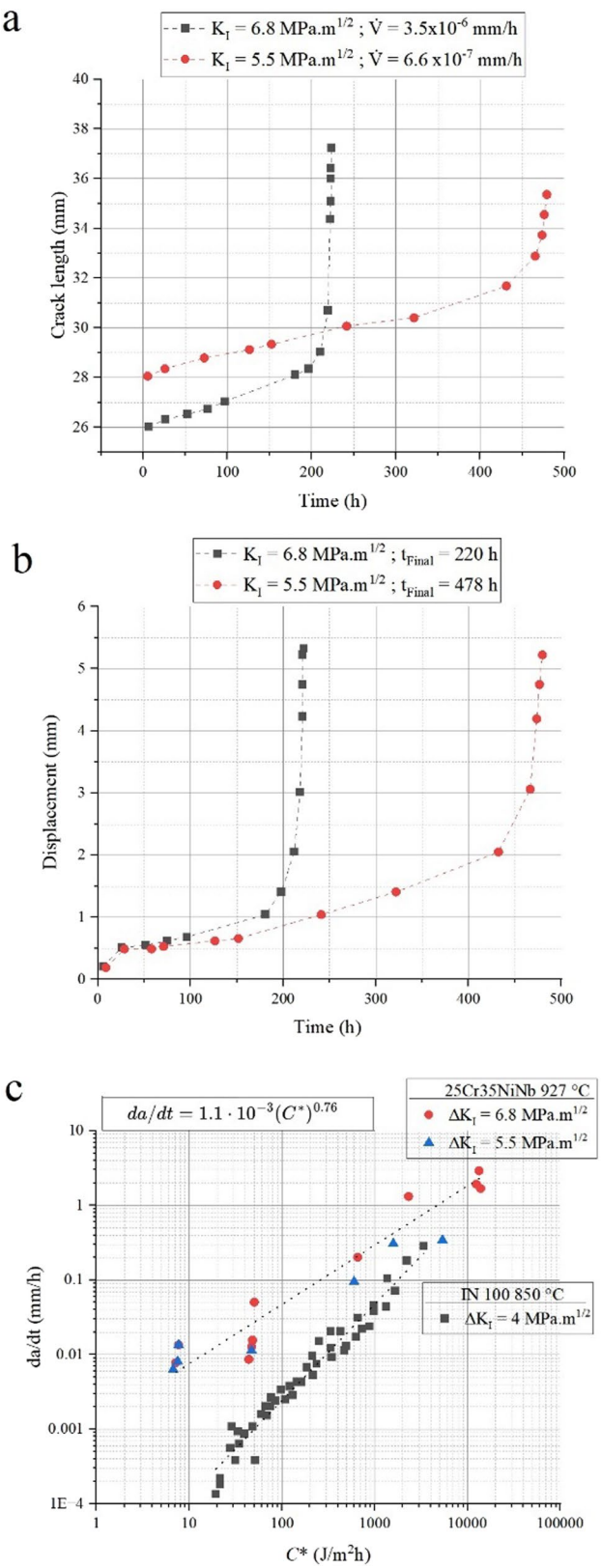

Fig. 19 **a** Curves of the crack length increase as a function of the test time for the AC condition in two initial stress intensity factors, i.e., K_I=6.8 MPa.m$^{1/2}$ and K_I=5.5 MPa.m$^{1/2}$. **b** Curves for increased load line displacement as a function of test time. **c** Relationship between the crack growth rate *da/dt* as a function of parameter *C** encompassing the stationary and tertiary stages of propagation

4 Final conclusions

It was observed that the aging heat treatment lasting 1000 h at 927 ºC provided the precipitation of secondary carbides ($Cr_{23}C_6$) in the austenitic matrix γ of the alloy and the presence of phase G. Thus, the aging heat treatment caused an intense precipitation in the interdendritic space, where chromium carbides coalesced and became coarser, while niobium carbides did not undergo significant changes in their morphology.

The hardness results demonstrated an increase in hardness of approximately 13.6% in the material that underwent thermal aging treatment for 1000 h (T1000) at a temperature of 927 ºC, when compared to the hardness of the material in the as-cast condition (AC).

In the tensile tests, it was observed that the thermal aging treatment (T1000) increased the value of the mechanical resistance parameters, when compared to the values obtained in the AC condition. It was noted that the mechanical resistance parameters, for AC and T1000 conditions, decreased with increasing test temperature and, on the other hand, ductility parameters increased with increasing temperature.

The results of the Charpy impact tests on V-notch specimens, carried out at 25 ºC, presented values lower than those obtained at 927 ºC in all tested conditions. The two conditions of the material studied (AC and T1000) were sensitive to the presence of a pre-crack nucleated by fatigue at the tip of the notch.

In conventional creep tests, small variations in the stress exponent (*n*) from the Norton Diagram were observed in the temperature range from 871 to 1066 ºC. It was noted that at the highest temperature of 1093 ºC, the stress exponent showed a sharp decrease, as a consequence of the alloy's high plasticity at that temperature.

Low-cycle fatigue tests showed that the transition life ($2N_t$) of the T1000 condition is greater at a temperature of 927 ºC due to its greater ductility than at 25 ºC. The fatigue life of the material tested at 25 ºC is much higher than the fatigue life at 927 ºC, especially in the high-cycle fatigue region. This fact can be attributed to two time-dependent factors: premature nucleation resulting from a significant reduction in the yield strength and/or the effect of surface oxidation of the permanent slip bands.

Fatigue crack propagation tests showed that the crack propagation rate *da/dN*, for each material condition, is higher at a temperature of 927 ºC than at 25 ºC, due to the greater ductility that the material presented at the elevated temperature. It was also noted that, at a temperature of 25 ºC, the fatigue crack propagation rate is higher in the T1000

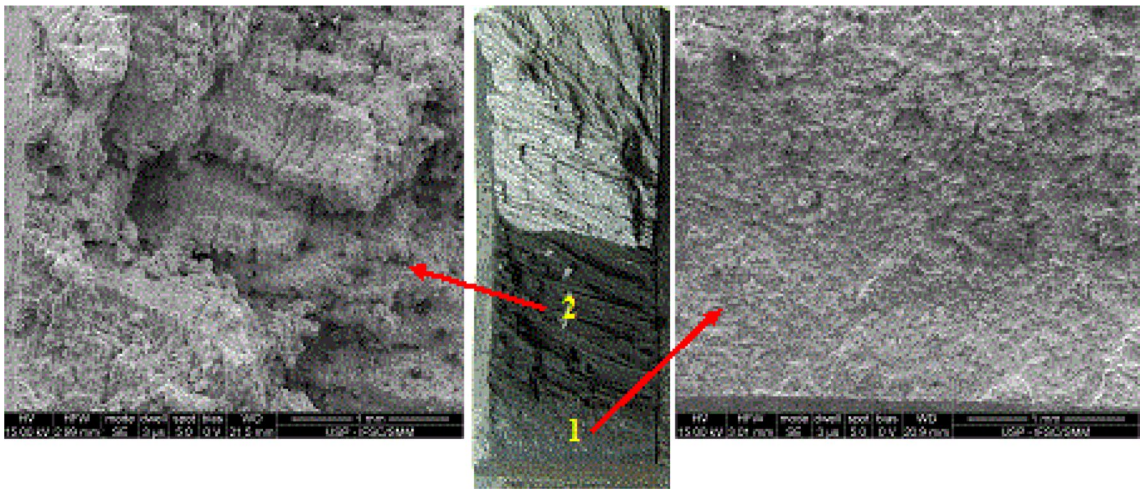

Fig. 20 Microfractographic aspects obtained in different regions in the fracture of the AC test specimen tested with $K_I = 6.8$ MPa.m.$^{1/2}$

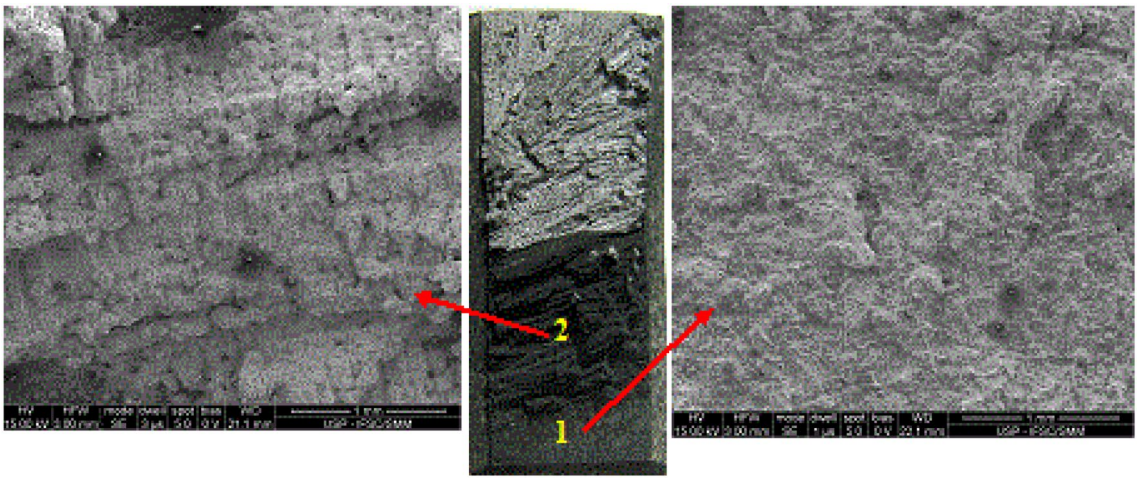

Fig. 21 Microfractographic aspects obtained in different regions in the fracture of the specimen of the AC condition tested with $K_I = 5.5$ MPa. m$^{1/2}$

material than in the AC, due to the large number of secondary precipitates existing in the austenitic matrix of the former. In tests at 927 ºC, no significant difference in behavior was noted for the two conditions AC and T1000.

Fractographic analysis of the fracture surfaces of the alloy under AC and T1000 conditions, tested in fatigue crack propagation at temperatures of 25 ºC and 927 ºC, revealed that the fracture mode at 25 ºC for the two microstructural conditions is different from those tested at 927 ºC. In general, materials tested at 25 ºC have a flatter fracture than that observed at 927 ºC. In the tests carried out at 927 ºC, a significant difference between the fracture modes in the two microstructural conditions was also not noticed: what is noticeable is a fracture with a more ductile appearance and with very sinuous crack propagation. From the observation of the oxides on the fracture surface of the specimens tested at high temperatures, it can be inferred that the oxidation process may have partially contributed to the operation of an intergranular (interdendritic) propagation process.

In the creep crack propagation tests, it was observed that the lower initial stress intensity factor (K_I) applied provided a decrease in the crack growth rate in the secondary stage when compared to the higher K_I value, a behavior as expected for a material in the as-cast condition.

The results of the creep crack propagation rate da/dt as a function of the C^* parameter, obtained by the experimental technique developed in this research project, allowed the proposal of the equation $da/dt = 1.1x10^{-3}(C^*)^{0.78}$, which can be applied to predict the life of components manufactured with the material studied in this project.

This work also concludes that the ASTM A297 Gr HP (25Cr35NiNb) alloy, with gross As-cast microstructure, presents creep crack propagation rates approximately 10 times higher for low C^* values than the superalloy of IN100 nickel, also in as-cast condition.

From the microfractographic analysis obtained in the pre-fatigue crack region, the planar morphological aspect typical of fatigue crack propagation carried out at room temperature can be noted. However, in the region of creep crack propagation, carried out at high temperature, a fracture morphology with the typical aspect of slow creep propagation can be observed, where an interdentritic morphology can be observed as well as a severe oxidation process, due to over a long period of time at a temperature of 927 ºC. This may also have contributed to an intergranular (interdendritic) propagation process, in which case the fracture surface shows brittle behavior, as expected for an as cast condition.

The experimental results obtained during this project's development provided values for two important parameters: monotonic mechanical resistance and the nucleation and propagation of fatigue and creep cracks. These parameters are crucial for characterizing the ability of ASTM A297 Gr HP alloy, which has been modified with Niobium, to resist crack initiation and propagation due to fatigue and creep mechanisms at high temperatures. This characterization is essential from the perspective of time-dependent fracture mechanics.

Acknowledgements The authors would like to thank Prof. Dr. Dirceu Spinelli, in memoriam, for his inspiration and dedication to work throughout his life. They express their gratitude to Engemasa company for the donation of the Creep Machine and for the supply of ASTM A297 Gr HP-Nb steel and to the research funding agencies CAPES (Proc. 23038038434/2008-33), CNPq (Proc. 301967/2010-5), and FAPESP for financial support.

Funding Coordenação de Aperfeiçoamento de Pessoal de Nível Superior

References

1. ASM handbook vol 1. (1993) ASM, Metals Park
2. Ray AK, Roy N, Raj A, Roy BN (2016) Structural integrity of service exposed primary reformer tube in a petrochemical industry. Int J Press Vessels Pip. https://doi.org/10.1016/j.ijpvp.2015.10.003
3. Bonaccorsi L, Guglielmino E, Pino R, Servetto C, Sili A (2014) Damage analysis in Fe–Cr–Ni centrifugally cast alloy tubes for reforming furnaces. Eng Fail Anal. https://doi.org/10.1016/j.engfailanal.2013.09.020
4. Attarian M (2016) Microstructural and failure analysis of welded primary reformer furnace tube made of HP-Nb micro alloyed heat resistant steel. Eng Fail Anal. https://doi.org/10.1016/j.engfailanal.2016.05.023
5. ASTM A297/A297M-19 (2019) Standard specification for steel castings, iron-chromium, and iron-chromium-nickel, heat resistant, for general application. ASTM international, West Conshohocken, PA. https://doi.org/10.1520/D5767-18
6. Olson DL (1985) Prediction of austenitic weld metal microstructure and properties. Weld J 2:281–295
7. Alvino A, Ramires D, Tonti A, Lega D (2014) Influence of chemical composition on microstructure and phase evolution of two HP heat resistant stainless steels after long term plant-service aging. Mater High Temp. https://doi.org/10.1179/0960340913Z.0000000001
8. Barbarella GD, Almeida LH, Silveira TL, May IL (1991) Phase characterization in two centrifugally cast HK stainless steel tubes. Mater Charact 26:1–7
9. Almeida LH, Ribeiro AF, May IL (2002) Microstructural characterization of modified 25Cr–35Ni centrifugally cast steel furnace tubes. Mater Charact. https://doi.org/10.1016/S1044-5803(03)00013-5
10. Shore FM, Morakabati M, Abbasi SM, Momeni A (2014) Hot deformation behavior of incoloy 901 through hot tensile testing. J Mater Eng Perform. https://doi.org/10.1007/s11665-014-0863-5
11. Tabatabaee SE, Mousavi-Anijdan SH, Najafi H (2021) Hot deformation mechanisms, mechanical properties and microstructural evolution of a HP-Nb steel. Mater Sci Eng, A. https://doi.org/10.1016/j.msea.2020.140326
12. Araújo MVP, Carvalho MC, Ruchert COFT (2021) Study of monotonic and cyclic mechanical behavior and microstructural evolution at a high temperature of ASTM A297 HP steel modified with niobium. J Eng Fail Anal. https://doi.org/10.1016/j.engfailanal.2021.105393
13. Liaw PK, Saxena A, Shaefer J (1997) Creep crack growth behavior of steam pipe steels effects of inclusion content and primary creep. Eng Frac Mec 57:105–130
14. Ashby MF, Browm LM (1983) Perspectives in creep fracture (Acta Metallurgica). Pergamon Press Ltd, Oxford
15. Zhang XZ, Wu XJ, Liu R, Liu J, Yao MX (2017) Deformation-mechanism-based modeling of creep behavior of modified 9Cr-1Mo steel. Mater Sci Eng A. https://doi.org/10.1016/j.msea.2017.02.044
16. Wu XJ, Zhang XZ, Liu R, Yao MX (2020) Creep performance modeling of modified 9Cr-1Mo steels with oxidation. Metall Mater Trans A. https://doi.org/10.1007/s11661-019-05588-0
17. Landes JD, Begley JA (1976) A fracture mechanics approach to creep crack growth. In: Mechanics of crack growth, ASTM STP 590, American Society for Testing and Materials, Philadelphia, pp 128–148
18. ASTM E-1457-13 (2007) Standard test methods for measurement of creep crack growth times in metals. ASTM International, West Conshohocken, https://doi.org/10.1520/E1457-19E01
19. Saxena A (1998) Nonlinear fracture mechanics for engineers. CRC Press LLC, New York
20. Davies CM, Kourmpetis M, O'Dowd N, Nikbin K (2006) Experimental evaluation of the J or C* parameter for a range of cracked geometries. In: Fatigue and fracture mechanics: 35th volume. ASTM International, West Conshohocken, https://doi.org/10.1520/STP45541S
21. ASTM E139-11 (2018) Standard test methods for conducting creep, creep-rupture, and stress-rupture tests of metallic materials. ASTM International, West Conshohocken, https://doi.org/10.1520/E0139-11R18
22. Jones MD, Dean DW, Hughes D, Davies CM (2020) A novel method for load line displacement rate partitioning in creep crack growth tests on type 316H stainless steel. Eng Fract Mech. https://doi.org/10.1016/j.engfracmech.2019.106689
23. Kumar Y, Venugopal S, Sasikala G, Parida PK, Moitra A (2018) A Study of creep crack growth behaviour of a type 316(N) stainless steel weld and its mechanism. Mater Sci Eng, A. https://doi.org/10.1016/j.msea.2018.06.096

24. Mehmanparast A, Davies CM, Dean DW, Nikbin K (2016) Effects of plastic pre-straining level on the creep deformation crack initiation and growth behaviour of 316H stainless steel. Int J of Pre Ves Pip. https://doi.org/10.1016/j.ijpvp.2016.03.013
25. Zhao J, Mo T, Nie D (2008) The occurrence of room-temperature creep in cracked 304 stainless steel specimens and its effect on crack growth behavior. Mater Sci Eng, A. https://doi.org/10.1016/j.msea.2006.09.151
26. Hong HU, Rho BS, Nam SW (2002) A study on the crack initiation and growth from δ-ferrite/γ phase interface under continuous fatigue and creep-fatigue conditions in type 304L stainless steels. Int J Fatigue. https://doi.org/10.1016/S0142-1123(02)00019-1
27. Konosu S, Mashiba H, Takeshima M, Ohtsuka T (2001) Effects of pretest aging on creep crack growth properties of type 308 austenitic stainless steel weld metals. Eng Fail Anal. https://doi.org/10.1016/S1350-6307(99)00047-3
28. Alsmadi ZY, Murty KL (2021) High-temperature effects on creep-fatigue interaction of the Alloy 709 austenitic stainless steel. Int J Fatigue. https://doi.org/10.1016/j.ijfatigue.2020.105987
29. Soares GDA et al (1992) Niobium additions in HP heat-resistant cast stainless steel. Mater Charact 29:387–396
30. Buchanan KG, Kral MV (2012) Crystallography and morphology of niobium carbide in As-Cast HP-niobium reformer tubes. Metall and Mater Trans A. https://doi.org/10.1007/s11661-011-1025-0
31. ASTM E92-03 (2013) Standard test methods for Vickers hardness of metallic materials. ASTM International, West Conshohocken, https://doi.org/10.1520/E0092-82R03
32. ASTM E-8M-11 (2009) Standard test methods for tension testing of metallic materials. ASTM International, West Conshohocken, https://doi.org/10.1520/E0008_E0008M-11
33. ASTM E-21-09 (2009) Standard test methods for elevated temperature tension tests of metallic materials. ASTM International, West Conshohocken, https://doi.org/10.1520/E0021-09
34. ASTM E-23-12 (2007) Standard test methods for notched bar impact testing of metallic materials. ASTM International, West Conshohocken, https://doi.org/10.1520/E0023-23A
35. ASTM E-606-12 (2004) Standard test method for strain-controlled fatigue testing. ASTM International, West Conshohocken, https://doi.org/10.1520/E0606_E0606M-12
36. Bananntine JA, Comer JJ, Handrok JL (1990) Fundamentals of metal fatigue analysis. Prentice Hall, New Jersey
37. ASTM E-647-13 (2013) Standard test method for measurement of fatigue crack growth rates. ASTM International, West Conshohocken, https://doi.org/10.1520/E0647-13
38. ASTM E2760-10 (2010) Standard test method for creep-fatigue crack growth testing. ASTM International, West Conshohocken, https://doi.org/10.1520/E2760-10
39. Garin JL, Mannheim RL (2009) Sigma-phase precipitation upon industrial-like heating of cast heat-resistant steels. J Mater Process Technol. https://doi.org/10.1016/j.jmatprotec.2008.07.026
40. Castro CSB, Gonzalez BM, Barbosa R (2008) Estudo do envelhecimento dinâmico em um aço Nb-Mn-Cr-Mo. Tecnologia em Metalurgia e Materiais. https://doi.org/10.4322/tmm.00502011
41. James MA, Newman JC (2003) The effect of crack tunneling on crack growth: experiments and CTOA analyses. Eng Fract Mech. https://doi.org/10.1016/S0013-7944(02)00131-5
42. Wu X (2019) Deformation and life evolution in crystalline materials: an integrated creep-fatigue theory. CRC Press, Boca Raton, FL
43. Laird C (1967) The influence of metallurgical structure on the mechanisms of fatigue crack propagation. In: Grosskreutz J (ed) Fatigue crack propagation,. ASTM STP (415), Philadelphia
44. Webster GA, Ainsworth RA (1994) High-temperature component life assessment. Chapman & Hall, London
45. Tabuchi M et al (1999) Results of a japanese round robin on creep crack growth evaluation methods for Ni-base superalloys. Eng Fract Mech. https://doi.org/10.1016/S0013-7944(98)00082-4